Marine Structures 89 (2023) 103405

Contents lists available at ScienceDirect

Marine Structures

journal homepage: www.elsevier.com/locate/marstruc

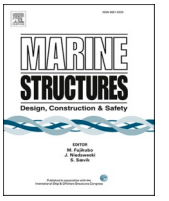

Effects of roughness on hydrodynamic characteristics of a submerged floating tunnel subject to steady currents

P.X. Zou [a,b,c], N. Ruiter [a], J.D. Bricker [a,c,*], W.S.J. Uijttewaal [a]

[a] Dept. of Hydraulic Engineering, Faculty of Civil Engineering & Geosciences, Delft University of Technology, 2600, GA, Delft, the Netherlands
[b] CCCC SFT Technical Joint Research Team, Zhuhai, Guangdong, 519080, China
[c] Dept. of Civil and Environmental Engineering, University of Michigan, Ann Arbor, MI, 48109, USA

ARTICLE INFO

Keywords:
Marine fouling
Hydrodynamic forces
CFD
Feature importance
Roughness parameters

ABSTRACT

The effects of surface roughness as induced by marine fouling on the hydrodynamic forces on a submerged floating tunnel (SFT) are experimentally and numerically investigated in detail at Reynolds numbers Re = 8.125×10^3–5.25×10^4. A sensitivity analysis to different roughness parameters including roughness height, skewness, coverage ratio, and spatial arrangement is performed. In addition, an optimized parametric cross-section for an SFT is proposed, and the hydrodynamic performance of the parametric shape and circular SFT cross-section shape with roughness elements is compared. The pressure distribution along the SFT, flow separation and wake characteristics are analyzed to provide a systematic insight [into the fundamental mechanism relating the roughness parameters and flow around an SFT. In order to better understand the nonlinear relationships among structural geometry, roughness parameters, flow states, and structural response, an artificial intelligence method using Random Forest (RF) for feature importance ranking is applied. The results show that with the parametric shape, the hydrodynamic forces on the fouled SFT can be effectively mitigated. The roughness height and coverage ratio affect the equivalent blockage and hence, change flow separation and recirculation length in the wake. Lower skewness of the roughness elements can increase the critical Re by changing the relative roughness parameter. Horizontal arrangement of the roughness elements on an SFT generally results in the largest hydrodynamic forces, compared to staggered and vertical distributions. Throughout the feature importance ranking, the flow regime is found to be the most important feature of the hydrodynamics of the SFT. In addition, the SFT cross-section shape and roughness coverage ratio play a dominant role.

1. Introduction

Marine biofouling, an accumulation of hard growth (e.g., mussels, oysters, barnacles), soft growth (e.g., seaweeds, sponges, anemones), and kelp growth (e.g. flapping weeds) is a major concern in the operational performance of submerged structures such as submerged floating tunnels (SFTs) [1,2]. Within years after construction, marine growth increases the effective dimension and mass of the SFT, which can have a substantial impact on the behavior of flow around the SFT by modifying the flow instabilities (e.g., vortex shedding, boundary layer separation) and hydrodynamic properties of a structure. This modifies the properties of the structure, e.g.

* Corresponding author. Dept. of Hydraulic Engineering, Faculty of Civil Engineering & Geosciences, Delft University of Technology, 2600, GA, Delft, the Netherlands.
E-mail address: j.d.bricker@tudelft.nl (J.D. Bricker).

https://doi.org/10.1016/j.marstruc.2023.103405
Received 14 November 2022; Received in revised form 4 January 2023; Accepted 31 January 2023
Available online 21 February 2023

buoyancy weight ratio of the SFT, and will therefore have direct effects on structural dynamic behavior (e.g., flow-induced vibrations [3], structural resonance, lock-in and synchronization [4]), affect the fatigue life, and bring difficulties to inspections for cracks and corrosion and for maintenance. According to Ref. [5], the roughness created by hard fouling is one of the main drivers for hydrodynamic changes. A limited number of studies have focused on the impacts of hard growth on the hydrodynamic behavior of marine structures, such as semisubmersible foundations [6], floating aquaculture cages [7], floating wind turbines [8], and jacket type offshore structures [9,10]. However, the effects of hard growth on hydrodynamic forces with varying roughness properties at different Reynolds numbers (Re) still remain unclear for an SFT.

Extensive experimental and numerical work has been performed to determine the effects of hard growth on circular cylinders; however, there is little consensus among these previous findings. Bearman and Harvey [11] concluded that both sand-roughened and dimpled cylinders have lower drag than smooth cylinders by lowering the critical Reynolds number (defined here as the Reynolds number at which the boundary layer transitions from laminar to turbulent). Similarly, Zhou et al. [12] compared different types of artificial surface roughness including sandpaper, netting, and dimples, and measured the force and flow characteristics of cylinders, concluding that the roughness elements can effectively reduce the mean drag coefficient of the cylinder. However, larger mean and fluctuating force values measured on a rough circular cylinder than those observed on a smooth one can be found in Refs. [13–15]. This can be attributed mainly to the differences in modelling set-ups and Reynolds number ranges [4]. In addition, structural end conditions, inlet turbulence intensity, blockage ratio, and aspect ratio have all been shown to be crucial factors in changing flow behavior and hydrodynamic forces [15–18].

In addition, the roughness parameter scale applied in the aforementioned research are not consistently determined, as the complexity of marine fouling characterization involves the definition of roughness parameter with uncertainties, which manifests in the definitions such as Reynolds number, drag and lift coefficients, and Strouhal number. There has not yet been a definite consensus on the determination of the roughness parameter from the literature. For instance, the bare cylinder diameter as an equivalent diameter was adopted in Ref. [15]; whereas, a bare cylinder diameter plus twice the average roughness height was adopted in Ref. [19]; the thickness of a closed volume with no water entrapment was defined in Ref. [14]. Nevertheless, the roughness parameter defined by an individual roughness length scale is not universal for all types of roughness. Some attempts to correlate different roughness types of fouled surfaces with measurable parameters have been performed. Achenbach and Heinecke [20] determined an equivalent pyramidal roughness parameter by introducing a critical Reynolds number. Abdelaziz et al. [21] developed simple geometric statistics for roughness based on a wide range of parameters such as mean roughness height, root mean square height, effective slope, skewness, and flatness. However, it is difficult to take into account all roughness distributions in a single measurable parameter since the effects of different roughness types are non-linear and highly related to flow regimes and instabilities [13]. Achenbach [22] also illustrated that a roughness parameter based on cylinder diameter as the reference length lacks physical meaning where the boundary layer thickness plays a dominant role.

Because of the existence of various types of marine organisms, the effects of different roughness parameters on the hydrodynamic forces on a marine structure and surrounding flow fields have been studied. Amongst these, roughness height is one of the most extensively studied factors [6,13–15]. Furthermore, Demirel et al. [23] and Schultz [24] showed that the hydrodynamic performance of structures is greatly dependent on the extent of coverage of fouling. In addition, Fuss [25] illustrated that skewness of the roughness elements further affects the force coefficients and critical Reynolds number. However, the relationship between hydrodynamic forces and roughness parameters is indirect, showing its complexity and nonlinearity in different flow regimes. Therefore, an importance ranking for roughness features is needed to provide more valuable insights into marine fouling effects and the structure's dynamic response, to provide guidance in engineering design, construction, and maintenance.

Based on the limitations of the previous studies, the objectives of the present study are, (1) to better identify and understand the effects of marine fouling on the hydrodynamic forces on an SFT; (2) to provide a systematic insight into the fundamental mechanism relating roughness characteristics and flows around an SFT, by analyzing the pressure distribution along the SFT, flow separation, and wake characteristics; and (3) to fill the gap in the literature ranking the relative importance of roughness parameters for impacts on the hydrodynamic forces. For (1) and (2), factors including roughness height, coverage ratio, and skewness are selected for a sensitivity analysis according to the existing literature. Furthermore, roughness patterns in the submarine environment are parameterized based on their spatial variance, to investigate the three-dimensional impacts of marine fouling on an SFT. Another limitation of existing studies is that they focus on the roughness effect of cylinders with simple cross-section shapes (e.g., circle, rectangle) only. Since the cross-section geometry of an SFT has a significant effect on flow behavior, Zou et al. [26,27] proposed an optimized parametric cross-section shape for an SFT in improving the hydrodynamic performance. Therefore, flow resistance due to marine fouling on an SFT with the parametric shape, is investigated and compared to simpler cross-section shapes; For (3), an artificial intelligence approach based on Random Forest (RF) is applied to rank the relative importance of roughness parameters.

The paper is structured as follows. The experimental set-up of SFTs with circular and parametric shapes in the steady current flume is described in Section 2. Sections 3 and 4 introduce the numerical modelling methodology and numerical validation, respectively. Section 5 quantifies the influence of different roughness parameters on the hydrodynamic forces on the SFT, followed by analysis of the effects of marine fouling on the flow behavior around the SFT. The relative importance of roughness features performed by RF is discussed in Section 6.

2. Experimental set-up

2.1. Flume and instrumentation

Physical model tests were performed in a wave-current flume at the Water Lab of Delft University of Technology (TU Delft) [28]. The flume has a length of 39 m, a width of 0.8 m, and a height of 1 m. The water depth is 0.70 m. Water surface elevation and current speed are measured by two arrays of resistance wave gauges and electromagnetic velocity meters (EMSs), respectively. An SFT with an internal diameter of 0.16 m is suspended from a stainless-steel frame with a strip stiffly connected to the flume top, leaving about a 2 cm gap to each side of the flume. The SFT model is placed horizontally with an additional weight tied to the strip to balance the net buoyancy. The submergence depth of the SFT is 0.35 m (measured from the center of the SFT to the free surface). A single point load cell from ME (type K3D60a) is mounted on the strip with a measuring range of ±100 N. The load cell can measure the total horizontal and vertical forces on the SFT simultaneously. The data sampling frequency is 200 Hz with a block size of 2 data points. The precision of the load cell is better than 0.5%. Flow visualization is conducted by injecting a fluorescent dye (Potassium permanganate) upstream of the SFT. Video recordings are taken with a Canon EOS 550D to capture wake structures and flow separations. The experimental apparatus is shown in Fig. 1.

2.2. Model fabrication

A regularly shaped roughness element is selected for a basic understanding of the marine fouling effects. The pyramidal roughness has a better set-up independency [4], and hence, is adopted in this study. Pyramids were fabricated with 3D printing technology. The pyramids have a base-height ratio of 2:1 with a height of 1.5 cm and cover the SFT with a coverage ratio of 100%. These roughness elements in the experiments are applied in a staggered arrangement, where the sheltering effect can be avoided. SFT slices are fabricated using silicon molding filled with epoxy. The SFT slices are assembled after solidification using silicon sealant and polyurethane foam to ensure waterproofing. Two types of cross-sections (circular and parametric) are investigated, to determine the impacts of fouled cross-section shapes on the hydrodynamic behavior of the SFT (Fig. 1 (b) and (c)). The heights of the two SFTs cross-section shapes are equal (i.e., 16 cm) to fix the flow blockage ratio. The equivalent diameter (D_e) of the rough SFT is determined by an equivalent blockage area, given by

$$D_{ex,ey} = D_{x,y} + 2k_s \tag{1}$$

where $D_{x,y}$ is the bare SFT dimension; Typically, the frontal area, which is the area projected on a plane normal to the direction of flow,

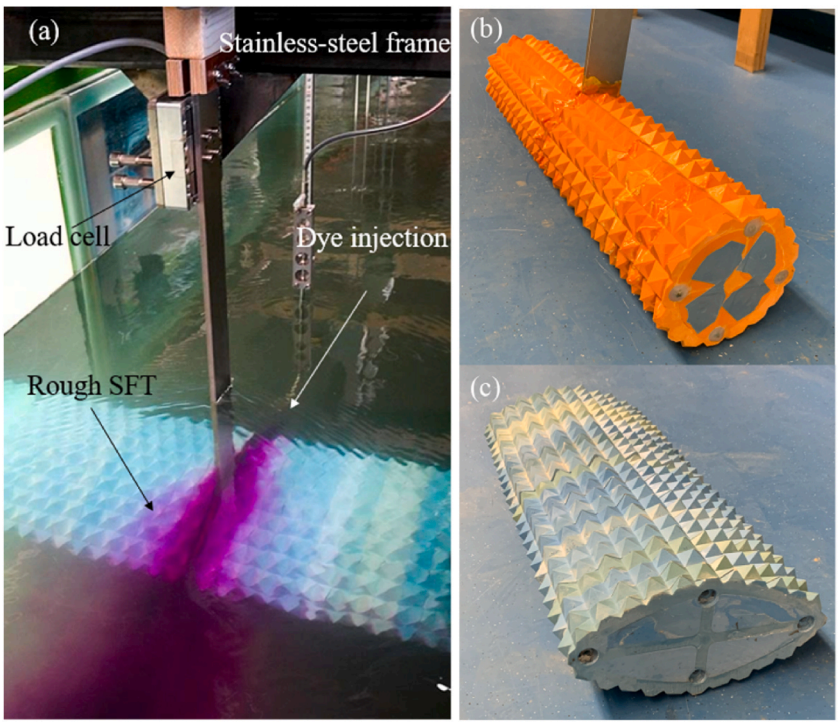

Fig. 1. (a) Experimental apparatus. Load cell attached to the SFT model, suspended from a stainless-steel frame, with an upstream dye injection for wake visualization (purple area); (b) Circular cross-section SFT model with roughness elements; (c) Parametric cross-section SFT model with roughness elements.

serves as the reference area for the drag coefficients. The planform area, or the area that would be visible from above in the direction normal to the bluff body, is typically used for lift coefficients calculation [29]. Therefore, in this study, the SFT height D_x is used for the drag coefficient while the SFT chord length D_y is used for the lift coefficient; k_s is the averaged roughness height with an equal blockage (reduced roughness height). With the equivalent diameter, the objective is to find a quadrangle that has the same blockage cross-sectional area as the original repetitive roughness elements, shown in Fig. 2.

Thus, the reduced roughness height k_s can be calculated by:

$$k_s = \frac{\sum_i S_i}{2l} \tag{2}$$

where S_i is the aera of a single roughness element; i is the number of repetitive roughness elements.

2.3. Experiment test cases

Table 1 summarizes the main conditions imposed on the experiments. The Reynolds number and the resulting of hydrodynamic forces are presented as a function of normalized coefficients, given by

$$\mathrm{Re} = \frac{\rho U D_{ex}}{\mu} \tag{3}$$

where U is freestream velocity; ρ is fluid density; μ is fluid dynamic viscosity.

The effects of marine fouling on the dynamic behavior of a submerged floating tunnel under currents can be characterized by the hydrodynamic coefficients, such as drag and lift coefficients. The mean drag coefficient ($C_{d,m}$) of the SFT is defined as

$$C_{d,m} = \frac{2F_{x,m}}{\rho U^2 D_{ex}} \tag{4}$$

where $F_{x,m}$ is the time-averaged drag force per unit of length.

The mean fluctuating lift coefficient ($C_{l,rms}$) of the SFT is defined as

$$C_{l,rms} = \frac{2F_{y,rms}}{\rho U^2 D_{ey}} \tag{5}$$

where $F_{y,rms}$ is the root mean square (RMS) fluctuating lift force per unit of length.

3. Numerical model set-up

In order to extend the experimental conditions and identify more roughness parameters' effects on the SFT, the influence of increased surface roughness as caused by marine fouling on an SFT is reproduced using Computational Fluid Dynamics (CFD) within the framework of the open source CFD toolbox OpenFOAM version 2006 [30].

3.1. Computational domain

The numerical results for current interactions with rough SFTs are validated against the experiments. In order to reproduce the experiments, validate the numerical results, and resolve the 3-dimensional roughness elements, 3-dimensional numerical models with different roughness parameters are established. The computational domain is 8 m in length and 0.7 m in height (equivalent to the water depth in the experiments). The center of the SFT is located 2 m from the inlet, with an internal flow blockage height (smooth SFT)

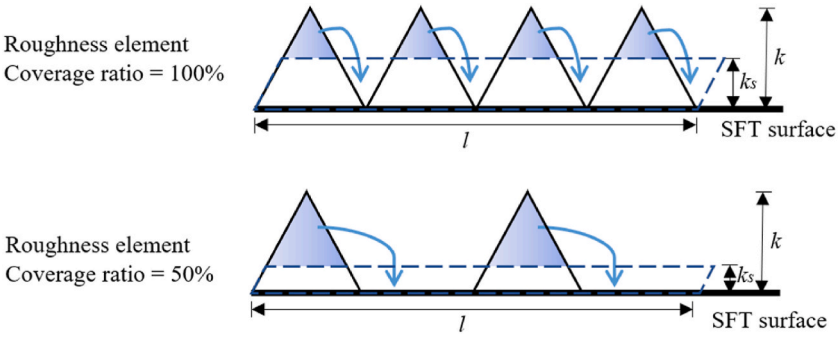

Fig. 2. Typical roughness patterns and reduced roughness height. k is the actual roughness height; k_s is the reduced roughness height with an equal blockage area; l is the length of the repetitive roughness patterns.

Table 1
Test conditions in the experiments.

	Test conditions
U (m/s)	0.1, 0.2, 0.3
Re	1.6×10^4, 3.2×10^4, 4.8×10^4
SFT cross-section	Circular, Parametric
Roughness height (cm)	1.5
Equivalent diameter (cm)	17.5
Coverage ratio (%)	100

of 16 cm. Due to the uniformly distributed roughness elements along the SFT span, the thickness of the numerical domain is determined by the length of the repetitive roughness pattern and truncated in the symmetry side planes with free-slip side boundaries, to assure coherence of flow structures over the SFT span. The typical grid layout is shown in Fig. 3. Freestream conditions for velocity and pressure are employed at both the inlet and outlet boundaries. The turbulence intensity at the inlet is 4%, which is consistent with the experiments. A simplified no-slip wall condition is applied on the SFT cross-section surface and at the bottom boundary. A free-slip wall is used at the upper boundary. A high-quality unstructured mesh is generated around the SFT cross-section surface. In order to capture the delicate fluid mechanics close to the SFT (i.e., boundary layer transition, flow separation, flow reattachment, wake characteristics, etc.), the boundary layer near the SFT surface should be well resolved. Therefore, the first grid layer cell length normal to the SFT surface (S_1) is chosen such that one wall unit y^+ is approximately 1. For the cell size near the bottom and top boundaries (S_2), a fine mesh with a grid resolution of 0.04 m is adopted. For the edges of the outlined zone near the SFT shown in Fig. 3 (b) (denoted by a red square), a cell size of 0.08 mm (S_3) is adopted, and a cell size in the rest of the domain (S_4) of 0.16 m is applied. The total number of cells ranges from 1.3 million up to 3.9 million, depending on the Reynolds number and roughness characteristics.

Schematized pyramid-shaped roughness elements reduce uncertainty associated with the complex biological processes involved, and a staggered pattern of roughness elements is designed to avoid sheltering effects. The influence of SFT cross-section shape, roughness height, and fouling coverage ratio on the hydrodynamic forces on an SFT are comparatively analyzed under various steady current conditions. Unsteady Reynolds Averaged Navier-Stokes (URANS) based transitional turbulence models are applied to investigate flow characteristics predictions such as flow separation, vortex shedding, and wake parameters. The transient solver PimpleFoam, supplied with OpenFOAM, for incompressible, turbulent flow is applied for steady current conditions. The merged PISO-SIMPLE (PIMPLE) algorithm is applied to solve the pressure–velocity coupling and correction. The maximum Courant number is set to 0.5. The initial time step was set to 0.01 s, followed by an adaptive time step based on the Courant number. The DelftBlue Supercomputer, a high-performance computing cluster, is applied to run parallel computation tasks [31]. 32 processes are executed in parallel per job.

3.2. Turbulence model

Zou et al. [32] reported that the Transition Shear Stress Transport (SST) model has the capability to accurately compute the hydrodynamic performance (e.g., separation-capturing and laminar-turbulent transition process) of an SFT at both low and high Reynolds numbers. The Transition SST model is based on the coupling of the k-ω SST transport equations with the intermittency and momentum-thickness Reynolds transport equations for the transition onset criteria [33,34]. In addition to the k and ω equations of the k-ω SST turbulence model, the additional transport equations of the Transition SST model are shown in Eq. (6)

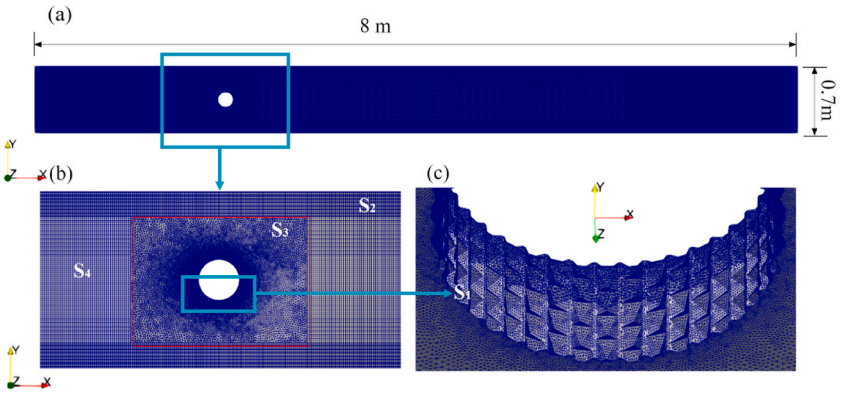

Fig. 3. Mesh configuration. (a) Computational domain of the numerical model; (b) Mesh detail near the SFT; (c) Mesh detail of roughness elements.

$$\begin{cases} \dfrac{\partial}{\partial t}(\rho\gamma) + \dfrac{\partial}{\partial x_j}(\rho\gamma U_j) = \dfrac{\partial}{\partial x_j}\left[\left(\mu + \dfrac{\mu_t}{\sigma_\gamma}\right)\dfrac{\partial\gamma}{\partial x_j}\right] + P_{\gamma 1} - E_{\gamma 1} + P_{\gamma 2} - E_{\gamma 2} \\ \dfrac{\partial}{\partial t}\left(\rho\widetilde{Re_{\theta t}}\right) + \dfrac{\partial}{\partial x_j}\left(\rho\widetilde{Re_{\theta t}}U_j\right) = \dfrac{\partial}{\partial x_j}\left[\sigma_{\theta t}(\mu + \mu_t)\dfrac{\partial\widetilde{Re_{\theta t}}}{\partial x_j}\right] + P_{\theta t} \end{cases} \tag{6}$$

where $\sigma_\gamma = 1.0$, and $\sigma_{\theta t} = 2.0$. μ_t is eddy viscosity. $P_{\gamma 1}$ and $E_{\gamma 1}$ are transition sources. $P_{\gamma 2}$ and $E_{\gamma 2}$ are destruction and relaminarization sources. $P_{\theta t}$ is production source term. γ is intermittency. $\widetilde{Re_{\theta t}}$ is transition momentum thickness Reynolds number.

The decay of the turbulent kinetic energy can be rewritten in terms of inlet turbulence intensity Tu_{inlet} and eddy viscosity ratio μ_t/μ as Eq. (7)

$$Tu = \left\{ {Tu_{inlet}}^2 \left[1 + \frac{3\rho V x \beta ({Tu_{inlet}}^2)}{2\mu(\mu_t/\mu)_{inlet}} \right]^{\frac{-\beta*}{\beta}} \right\}^{0.5} \tag{7}$$

where $\beta = 0.09$, and $\beta^* = 0.0828$. V is mean convective velocity. x is streamwise distance downstream of the inlet.

3.3. Grid independent limit (GIL) test

The mesh of the computation domain is generated by the ANSYS Mesh utility [35] and conversion to OpenFOAM compatible format is implemented by using the command *fluent3DMeshToFoam*. By assessing four grid configurations, the size and distribution of the mesh are determined by comparing the variation of the wall y^+ normal to the SFT surface, $C_{d,m}$, and $C_{l,rms}$ of the SFT. The GIL results are shown in Table 2 for the case of the circular SFT with a roughness height of 1.5 cm under a crossflow velocity of 0.3 m/s. It shows that the wall y^+ values in Case 3 and Case 4 are around 1, and the differences in $C_{d,m}$, and $C_{l,rms}$ values between the two cases are minor, so the convergence of mesh size is concluded to be achieved. Since Case 3 has fewer mesh cells, it is chosen for further simulations. It should be noted that the cell size of S_1 is determined by ensuring the wall y^+ is around 1 and varies with Re.

3.4. Numerical model test cases

In order to investigate the effects of marine fouling induced roughness on the hydrodynamic forces on the SFT and extend the test conditions in the experiments, a sensitivity analysis of roughness parameters including roughness height, skewness, coverage ratio, spatial arrangement, and cross-section shape is numerically carried out. The roughness parameters are shown in Table 3 and Fig. 4. Roughness skewness describes asymmetry and distortion characteristics of a given roughness distribution by measuring the deviation of a random variable from a symmetric distribution. The definition of the skewness parameter S_k is given by

$$S_k = \frac{n}{(n-1)(n-2)} \frac{\sum_{i=1}^{n}(k_i - k_m)^3}{s^3} \tag{8}$$

where n is the number of measured points along the circumference of the roughness profile; k_i is the height of the ith data point of the roughness profile; k_m is the sample mean roughness height; s is the sample standard deviation, given by

$$s = \left[\frac{1}{n-1} \sum_{i=1}^{n}(k_i - k_m)^2 \right]^{\frac{1}{2}} \tag{9}$$

4. Model validation

4.1. Forces on the SFT

The numerical results for the mean drag coefficient for the SFT with a roughness height of 1.5 cm for circular and parametric cross section shapes are plotted against Re and compared with experimental data (with error bars) in Fig. 5.

The maximum relative error is 9.1% at $R_e = 1.75 \times 10^4$ for the parametric cross section. This may be attributed to model end conditions, measurement error, experimental uncertainties, roughness pattern irregularities, or numerical assumptions. It should be noted that a fully 2-dimensional flow along the span of the SFT can hardly be achieved in the experiments due to end wall effects and

Table 2
Mesh sizes used in the GIL test.

	S_1	S_2	S_3	S_4	number of cells	Y^+	$C_{d,m}$	$C_{l,rms}$
Case 1	1 mm	8 mm	16 mm	16 mm	1,265,881	3.82–6.67	1.887	1.224
Case 2	1 mm	4 mm	8 mm	16 mm	1,730,324	2.28–4.43	1.892	1.228
Case 3	0.6 mm	4 mm	8 mm	16 mm	3,869,038	1.34–2.01	1.934	1.249
Case 4	0.6 mm	4 mm	8 mm	8 mm	4,075,150	1.21–2.03	1.931	1.247

Table 3
Model parameters.

Model conditions	
Current speed U (m/s)	0.05, 0.1, 0.2, 0.3
SFT cross-section shape	Circular, Parametric
SFT bare height (cm)	16
Roughness parameters	
Roughness height k (cm)	0.5, 1.0, 1.5
Roughness coverage ratio (%)	25, 50, 100
Roughness arrangement/Inclined angle (deg.)	0, 45, 90
Roughness skewness (−)	−1, +1

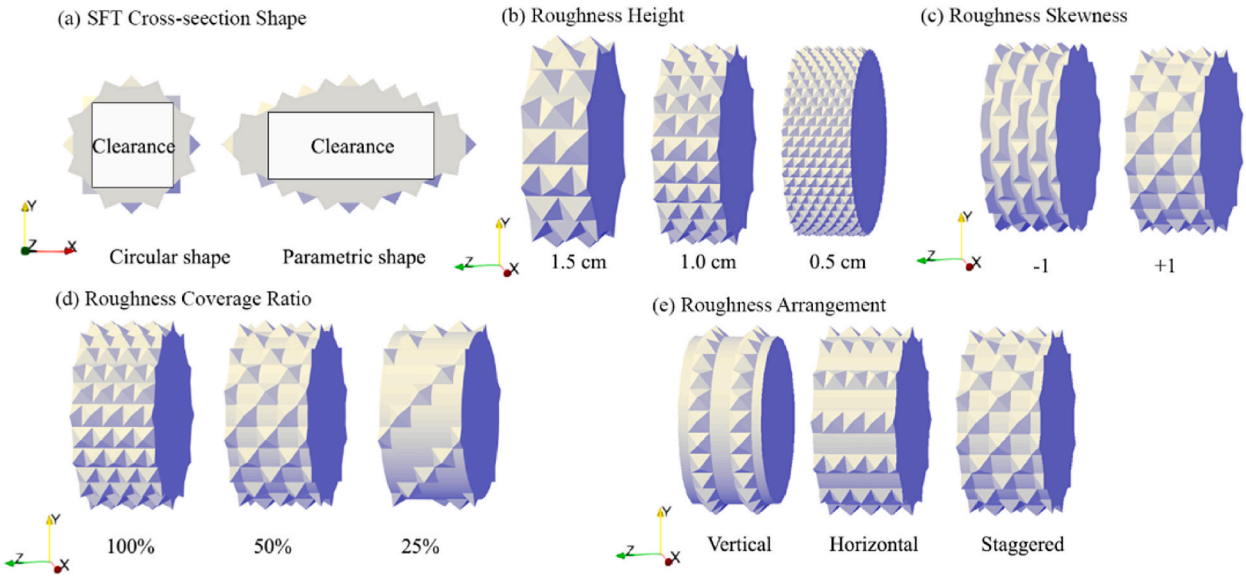

Fig. 4. SFT shapes and roughness parameters.

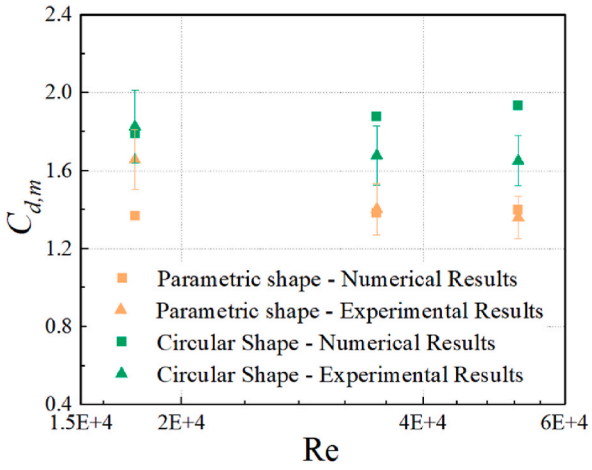

Fig. 5. Hydrodynamic force coefficient validation.

the small aspect ratio of the SFT applied in this study (SFT length/width is around 5). West and Apelt [16] investigated the aspect ratio effects on the hydrodynamic forces of a cylinder, and found that for a given blockage ratio, the drag coefficients decrease with increasing aspect ratio. However, the relative difference of the drag coefficients between the aspect ratio of 5 and 22 is within 4%, indicating that the aspect ratio induced 3-dimensional flow effects in this study is minor. Furthermore, by leaving the gap to each side of the flume, the boundary layer effects at the end wall can be partially mitigated, and it is a common treatment strategy in

2-dimensional experiments [36,37]. There are other attempts such as using endplates assembled at the end of the SFT [38]. With the endplates, spanwise uniformity of mean conditions can be achieved by preventing the three-dimensional flow. However, the endplates can unavoidably introduce 'second-order' end effects, which can contribute to the formation of 3-dimensional structures in the wake [16]. It is still challenging for the 2-dimensional experiments to avoid the end wall effects. In addition, the free surface in the numerical models is excluded. Reichl [39] numerically investigated flow past a cylinder close to the free surface with various gap ratios h/D (i.e., the distance of the cylinder and the position of the undisturbed surface/cylinder diameter), and found that the Strouhal number increases in the range $0.5 < h/D < 1.0$ with an enhancement of around 10%, while it mildly changes as the gap ratio increases above 1. For small gaps ($h/D < 1.0$), the convective velocity of the vortices of each side of the cylinder is unequal, and surface vorticity causes a significant change in wake dynamics. However, as the gap ratio increases, the convective velocity of the negative vortices approximately equal to the positive vortices, indicating the free surface effects can be negligible for deep submergence. As the gap ratio of the SFT is 1.7 in this study, the free surface effects are not substantial. However, an appropriate quantitively analysis is suggested for the future work. Therefore, the order of magnitude of the drag coefficients is a reasonable agreement, implying the validity of the numerical results.

Since vortex shedding is not uniformly distributed along the SFT but occurs in cells, lift forces measured over the entire cylinder in the experiments experience low spanwise correlation effects; therefore, the lift coefficients obtained from the numerical results for a short slice of SFT tube, and experimental data for a long tube, are not directly comparable.

4.2. Vortex shedding comparison

Fig. 6 shows the morphology of the vortex street at $\mathrm{Re} = 3.3 \times 10^4$ for circular and parametric cross-section shapes. This time instant corresponds to the lift reaching its peak value. In the experiments, the dye is swept into vortices behind the SFT, forming large coherent structures as they move downstream away from the SFT. These large coherent structures indicate the locations of concentrated vorticity. In the numerical model, vortices in the wake are resolved. The shedding process begins with the recirculation zone behind the SFT moving from one side to the other (e.g., downwards to upwards), the rear part of the recirculation zone at that side will form the first shed vortex, and push the recirculation zone of the other side away from the SFT, to generate the second vortex. The widening of the wake can be seen as the spreading of these vortices, and a periodically steady-state shedding of the vortices is found.

From Fig. 6, the vortex shedding in the numerical models is generally consistent with the experimental results. Interestingly, it can be observed from both the numerical and experimental results that vortices shed behind the SFT grow larger in size with the circular

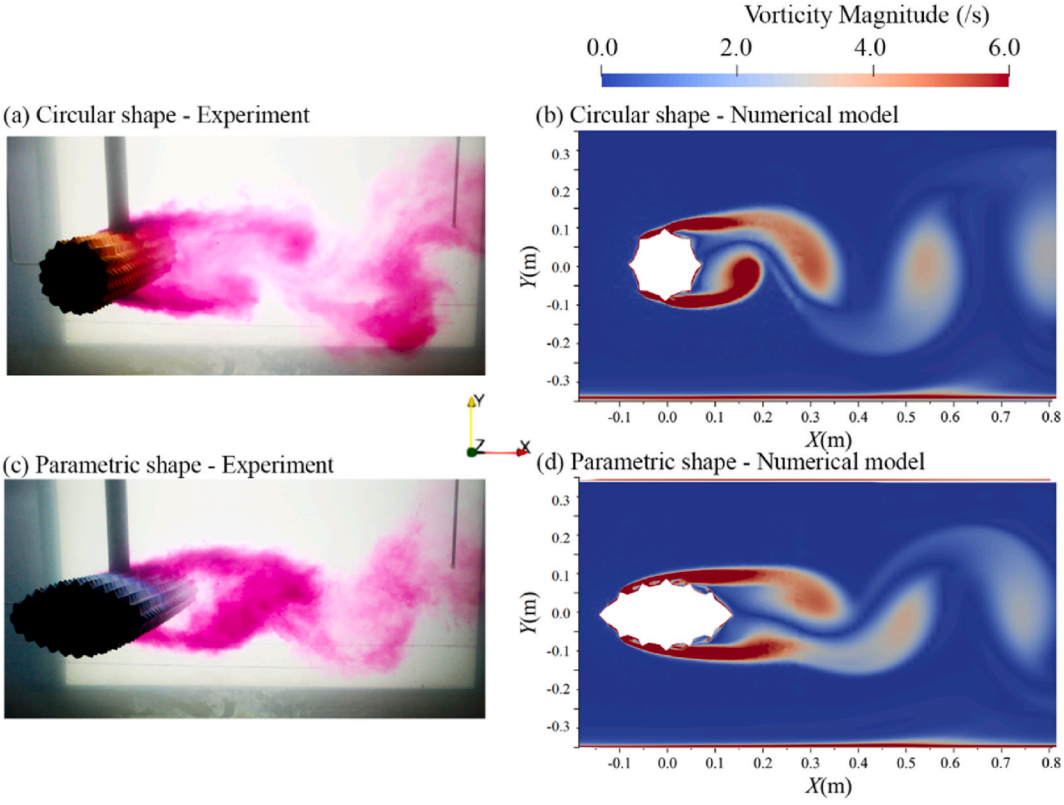

Fig. 6. Flow visualization at $U = 0.2$ m/s (a) circular rough SFT in the experiments; (b) circular rough SFT in the numerical model; (c) parametric rough SFT in the experiments; (d) parametric rough SFT in the numerical model.

cross section, compared to the parametric cross section. Furthermore, vortices grow larger in the region further downstream away from the SFT with the circular cross section (i.e., closer to the bottom and free surface). It should also be noted that the formation length of the recirculation region behind the SFT in the numerical models is shorter than in the experiments. RANS turbulence models using turbulence eddy viscosity, tend to over-estimate turbulence in the vortex cores, inducing a more rapid diffusion of the initially concentrated vorticity [40].

5. Results analysis

5.1. Effect of SFT cross-section shape

Cases of circular and parametric SFT cross section shapes with a fixed roughness height of 1.5 cm and coverage ratio of 100%, staggered roughness arrangement, and roughness skewness of +1 are selected, to investigate the effects of the cross-sectional shape on the hydrodynamic forces on the SFT (Fig. 4(a)).

The mean drag coefficient $C_{d,m}$ and RMS fluctuating lift coefficient $C_{l,rms}$ for the two shapes are plotted against Re in Fig. 7. It shows that over the selected Re range, $C_{d,m}$ is generally around 1.86 and 1.38, for the circular shape and parametric shape, respectively, and variations are not obvious. Note that for an equal blockage height, the parametric shape has a much lower $C_{d,m}$, compared to the circular shape. For computing $C_{l,rms}$, the blockage in the streamwise direction is selected as the equivalent diameter, inducing a remarkable drop of $C_{l,rms}$ with the parametric shape. In general, $C_{d,m}$ and $C_{l,rms}$ can be effectively reduced by around 26% and 82%, respectively, by adopting the parametric shape. Furthermore, as the SFT is mainly designed for transportations, the traffic volume for the SFT cross-section should be considered properly. The clearance within the parametric shape for road or rail transportation is much larger than that within the circular shape under equal blockage height, thereby increasing space utilization (Fig. 4(a)).

Streamwise mean velocity contours behind SFTs with circular and parametric cross-section shapes at $U = 0.1$ m/s are shown in Fig. 8, where the slice in the X–Y plane with the largest SFT flow blockage is presented. It is found that the local flow separation (i.e., reverse flow) occurs leeward of roughness elements on the windward side of the SFT for both shapes. For the circular shape, as the subsequent flow passes over the tip of the roughness element on the apex, the flow fully detaches from the SFT surface, leading to the development of free shear layers and the formation of a large recirculation zone behind the rear of the SFT (i.e., wake). However, for the parametric shape, when the flow passes over the tip of the roughness element on the apex, despite the local separation leeward of the roughness pyramid, the main stream seems still to be attached, separates further downstream, and generates a narrower wake region, compared to the circular shape.

The recirculation length is measured from the center of the SFT to the trailing stagnation point, where the streamwise mean velocity changes sign on the centerline. The recirculation length is highly related to the size of the vortices shed behind the SFT and the drag on the SFT. Fig. 8 shows that the recirculation length of the parametric shape is longer, due to its more streamlined shape and the longer chord length. Nevertheless, after subtracting the chord length, the wake length and width of the parametric shape are much shorter; moreover, the narrower separation of the free shear layer produces a weaker fluctuation of lift in the near wake. Therefore, the parametric shape drastically reduces drag and fluctuating lift coefficients in steady flow.

Fig. 9 displays the distribution of the time-averaged pressure coefficient $C_{p,m}$ along the Y direction on the SFT surface with the same slice in Fig. 8 for different cross-section shapes. The definition of $C_{p,m}$ is given by

$$C_{p,m} = \frac{2(p - p_{ref})}{\rho U^2} \tag{10}$$

where p is the static pressure along the SFT surface; p_{ref} is the reference pressure.

Due the symmetric shape of the cross section, $C_{p,m}$ is shown only on the upper part of the SFT cross-section. The influence of

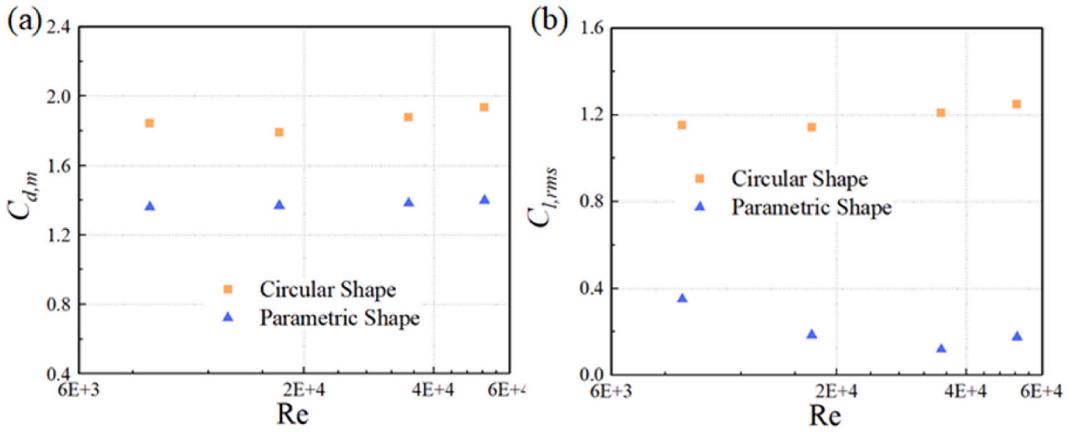

Fig. 7. Simulated hydrodynamic force coefficients for different cross-section shapes. (a)$C_{d,m}$ vs R_e;(b)$C_{l,rms}$ vs R_e.

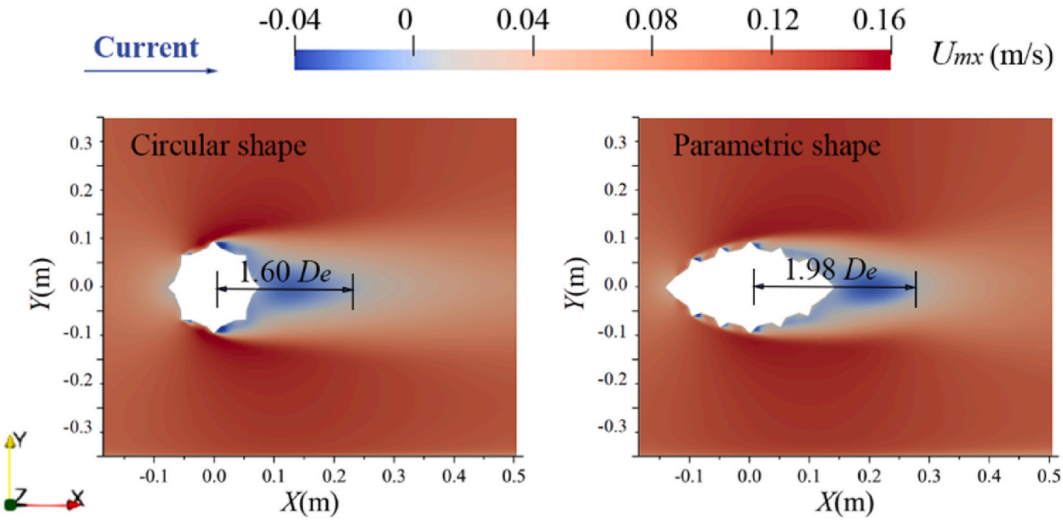

Fig. 8. Time-averaged streamwise velocity contours for rough SFTs with different cross-section shapes, $U = 0.1$ m/s.

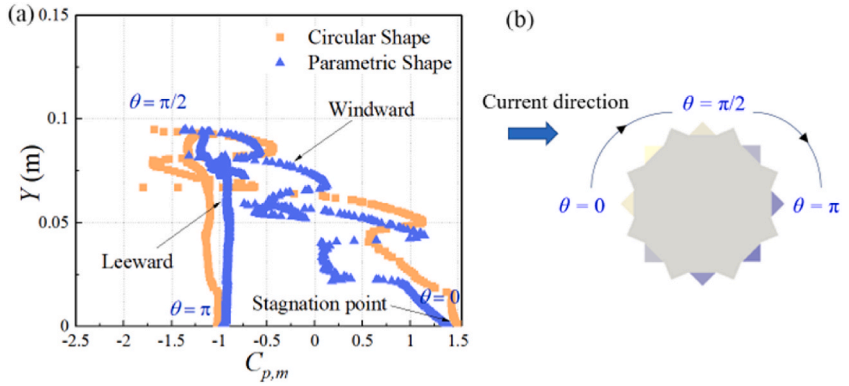

Fig. 9. (a)Time-averaged pressure coefficients for different cross-section shapes, $U = 0.1$ m/s; (b) Angle around the SFT surface, for marking the location of the pressure coefficient.

blockage on the hydrodynamic forces has been described in Ref. [18] that blockage ratio affects the pressure distribution, the occurrence of flow separation, and the nature of three-dimensional wake features by constraining the wake flow. In addition, the local flow velocity can be increased with an increasing blockage ratio. Since the blockage ratio of the SFT in this case is 25%, the large confinement of the boundary increases the local tangential velocity along the SFT surface and hence, increases the total pressure at the inlet before the steady state has been achieved. Thus, $C_{p,m}$ at the stagnation point reaches much higher than 1 (around 1.5 in this case). Moreover, the large blockage ratio also changes the near and far wake flow, which has an impact on lateral spreading of the free shear layers and the hydrodynamic force coefficients. However, the blockage ratio correction procedure cannot be simply applied, since the actual shape of the pressure distribution changes with blockage [16], which those methods (e.g., image method [41] and momentum method [42]) fail to take into account. Therefore, no blockage correction is used in this study.

Surface irregularity due to the roughness imparts three-dimensionality to the flow fields, and affects the pressure distribution along the SFT. After the flow passing over the stagnation point (i.e., the tip of the first pyramid at the leading-edge) at the windward edge of the SFT, the parametric shape experiences a generally smaller $C_{p,m}$ than the circular shape, due to its shorter local projected area and more streamlined shape. The $C_{p,m}$ in both cases decreases considerably around the leading-edge due to the increases in the flow velocity and the pressure gradient. As the flow passes the windward edge of the second pyramid, the local maximum velocity is reached at Y = 0.38 m and 0.44 m, for the parametric and circular shapes, respectively. Followed by an abrupt change in geometry when the flow confronts the windward side of the second pyramid's surface, the sudden curvature alteration leads to a change in the surrounding flow direction, and hence, an enhancement of the pressure on the SFT surface. When the flow direction turns to be parallel to the pyramid's surface at the windward edge, the flow keeps accelerating until the pressure drops to its local minimum (suction) when the flow passes over the tip of the second pyramid at around Y = 0.059 m and 0.067 m, for the parametric and circular shapes, respectively.

With the onset of local flow separation induced by a strong adverse pressure gradient (APG), $C_{p,m}$ experiences a sharp increase and reaches its local maximum near the leeward base of the second roughness pyramid. The sharp corners can trigger flow separation when

viscous forces near the SFT wall are overcome by the flow momentum, causing a zero flow velocity near the boundary and local detachment of the fluid. Likewise, $C_{p,m}$ experiences a dramatic decrease between the second and the third roughness pyramids and reaches its local minimum at around Y = 0.055 m and 0.079 m, for the parametric and circular shapes, respectively. The decrease in $C_{p,m}$ is found to be identical in both cases, due to the equal roughness heights and aspect ratios. Again, $C_{p,m}$ undergoes a sudden jump (i.e., a sharp increase followed by a decrease) when it passes over the windward surface of the third roughness pyramid. However, the rates of increase and decrease of $C_{p,m}$ are found to be smaller than in the previous jumps, which can be attributed to energy losses (dissipation) in the system and flow separation by the abrupt pressure conversion. With the parametric cross section's longer perimeter, the additional roughness pyramid induces one more pressure jump at the windward surface than the circular shape experiences. When the flow passes over the tip of the pyramid at the apex of the cross section, $C_{p,m}$ reaches its local minimum of −1.35 and −1.65, for the parametric and circular shapes, respectively, followed by another jump (but a slight increase and decrease of $C_{p,m}$ when the flow interacts with the leeward pyramids). The local flow acceleration due to the alternation of geometry has a negligible impact on the pressure distribution after the mainstream flow separation. Therefore, leeward of the SFT surface, despite the small fluctuations of $C_{p,m}$ due to the flow interaction with roughness elements, the $C_{p,m}$ distribution remains almost constant within the wake region. However, greater fluctuation of $C_{p,m}$ can be observed in the circular shape. The base pressure coefficients $C_{p,bm}$ are −1.1 and −0.9, for the parametric and circular shapes, respectively. A smaller pressure drop between the front and rear of the SFT with the parametric shape is seen to effectively reduce the drag and lift, compared to the circular shape.

5.2. *Effect of roughness height*

Cases of roughness height k = 0.5 cm, 1.0 cm, and 1.5 cm covering an SFT cross section with a circular shape, an equal roughness coverage ratio of 100%, staggered roughness element arrangement, and roughness skewness of +1 are selected, to investigate the effects of the roughness height on the hydrodynamic forces on the SFT (Fig. 4(b)). The value of $C_{d,m}$ with respect to the Re for a smooth cylinder under steady currents is approximately constant before the drag crisis, namely the subcritical Re range, followed by a steep drop of Cd,m in the critical regime), while Cd,m plateaus in the super-critical region. After Cd,m drops to its minimum value, Cd,m increases in the upper-transition region, and is nearly constant at *trans*-critical Re [43]. The relationship between Cd,m and Re encompassing subcritical, critical, super-critical regimes, upper-transition, and *trans*-critical Re is shown in Fig. 10.

Fig. 11 shows $C_{d,m}$ and $C_{l,rms}$ vs. R_e for different roughness heights. It can be seen that $C_{d,m}$ and $C_{l,rms}$ decrease with increasing R_e in the k = 0.5 cm case, which is a characteristic trait for flow that transitions from the subcritical (before drag crisis) to the critical regime. The low values of $C_{d,m}$ and $C_{l,rms}$ observed at $R_e = 1.7 \times 10^4$ might be a signature of a critical regime followed by a super-critical regime and an upper transition (the two regimes can be merged in case of a rough wall [43]) in the k = 1.0 cm case. For k = 1.5 cm, $C_{d,m}$ and $C_{l,rms}$ are approximately constant regardless of Re, which might be an indication of the *trans*-critical regime throughout the investigated Re range. It is well accepted that perturbation of the flow by roughness can promote an earlier transition to a turbulent boundary layer, causing the critical regime (i.e., drag crisis) to occur at a smaller Re, and the critical Re decreases with increasing roughness height. The larger roughness height generates a thicker boundary layer, where the weaker momentum exchange near the wall induces a larger separation angle, and hence, facilitates earlier transition and increases the drag coefficient. Therefore, $C_{d,m}$ and $C_{l,rms}$ increase as the roughness height increases. The relationship between critical Re and the roughness parameter of a rough cylinder can be approximated by [20].

$$\mathrm{Re}_{crit} = \frac{6000}{(k_s/D)^{\frac{1}{2}}} \tag{11}$$

where k_s is Nikuradse equivalent sand roughness.

Assuming that k_s in equation (11) is equal to roughness height in this study, by deriving the roughness height k = 1.0 cm case, the critical Re can be estimated as 2.4×10^4, which is slightly over-estimated compared to the numerical results (Fig. 11). This discrepancy

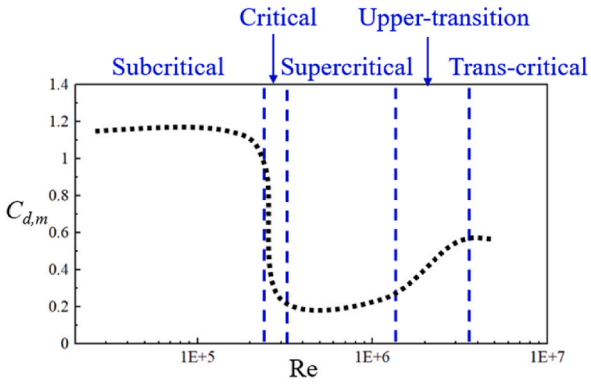

Fig. 10. Drag coefficient as a function of Re for a smooth circular cylinder, following [44].

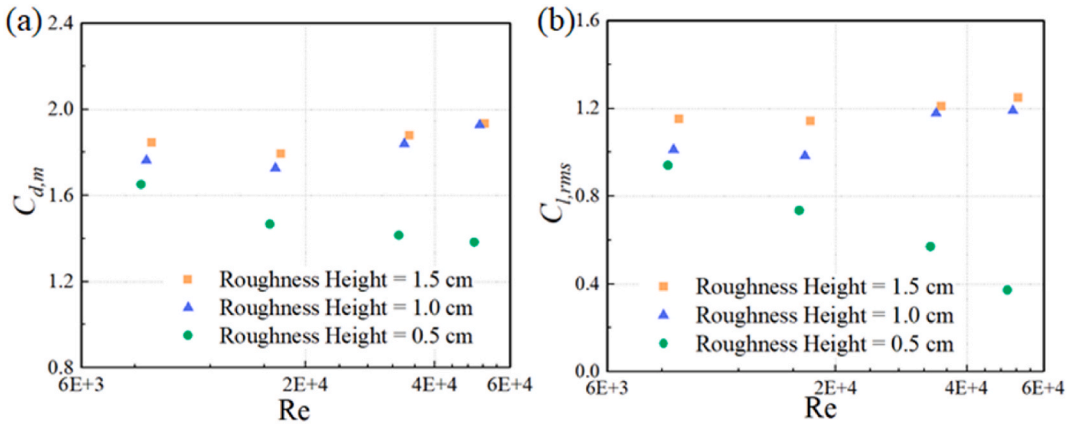

Fig. 11. Simulated hydrodynamic force coefficients for different roughness heights. (a)$C_{d,m}$ vs R_e;(b)$C_{l,rms}$ vs R_e.

can be partially ascribed to the roughness parameter assumption and large blockage in this study (large blockage can trigger earlier critical transition [45]). However, it can provide a basic and straightforward method of critical Re prediction for a rough cylinder.

Interestingly, notice that at an equal Re, although $C_{d,m}$ and $C_{l,rms}$ increase with increasing roughness height, the rate of increase of $C_{d,m}$ and $C_{l,rms}$ slows down. This behavior is closely related to the flow state and boundary layer behavior, which will be addressed in more detail hereafter.

The mechanism underlying the variation of $C_{d,m}$ and $C_{l,rms}$ with the roughness height can be interpreted from the mean streamwise velocity contour around the SFTs in Fig. 12. The slice of the SFT shown is selected as that with the largest blockage in the X–Y plane with $U = 0.1$ m/s. It clearly shows that the cross-stream spacing of the wake and recirculation length increase with increasing roughness height due to the increase of blockage, and thus, enhances the drag. However, the relationship between fluctuating lift coefficient and the wake parameters are complex [46]. As can be seen, the flow separation point in each of the three cases occurs generally at the roughness element tips on the apex and nadir of the SFT. Due to the exaggerated roughness height and 3-dimensional properties of the roughness elements, the presence of the roughness distorts the streamline, detaches the flow from the SFT surface, and creates a large low-pressure, reverse flow area behind the SFT (i.e., wake). As a consequence, a large pressure drop forms between the front and rear surfaces of the SFT.

Fig. 13 displays the time-averaged pressure coefficient $C_{p,m}$ distribution in the Y direction on the SFT upper surface at the slice of the SFT with the largest blockage, for different roughness heights with $U = 0.1$ m/s. As can be seen on the windward half of the SFT, the amplitude of fluctuation of $C_{p,m}$ increases with increasing roughness height. Jumps in $C_{p,m}$ correspond to the number of roughness elements. The $k = 1.5$ cm case shows a larger variation of $C_{p,m}$ amplitude, while the $k = 1.0$ case, with more distributed roughness elements (Fig. 4 (b)), has yet more $C_{p,m}$ jumps. The pressure distribution over the windward half of the SFT is a combined effect of the two factors. Therefore, $C_{d,m}$ exhibits similar values in Fig. 11 for both cases (and the rate of increase of $C_{d,m}$ is slow). Nevertheless, despite the existence of more roughness elements (pyramids) in the $k = 0.5$ cm case, $C_{p,m}$ is seen to be much smaller than the other two cases over the windward portion of the SFT, which is the main reason for the sharp drop of $C_{d,m}$ in Fig. 11 (a). Comparing the base pressure coefficients on the leeward portion of the SFT, the three cases display fairly similar values. However, the $k = 1.5$ cm case shows a slightly larger $C_{p,m}$ (less suction) than the $k = 0.5$ cm case, followed by the $k = 1.0$ cm case. It can be furthermore stated that the

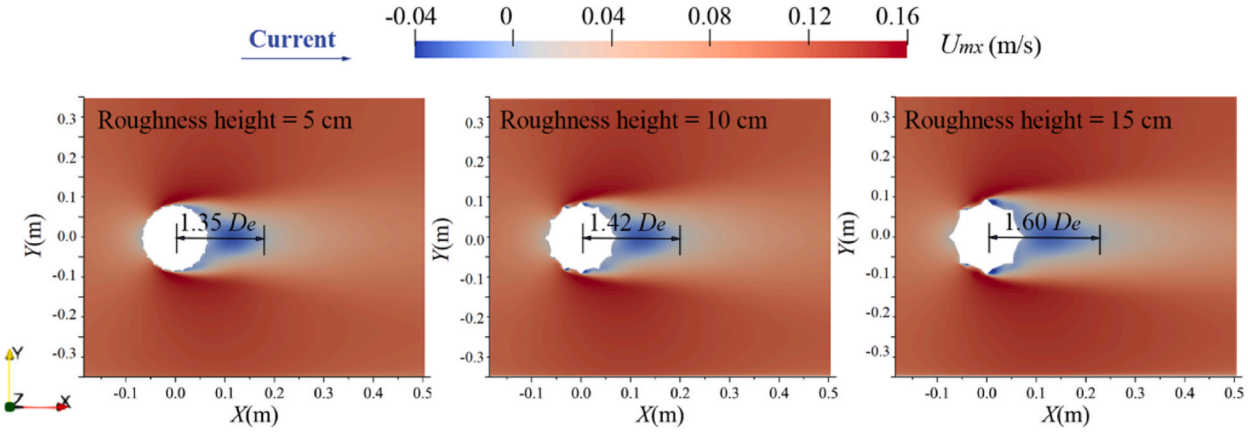

Fig. 12. Mean velocity contours of rough SFTs with different roughness heights, $U = 0.1$ m/s.

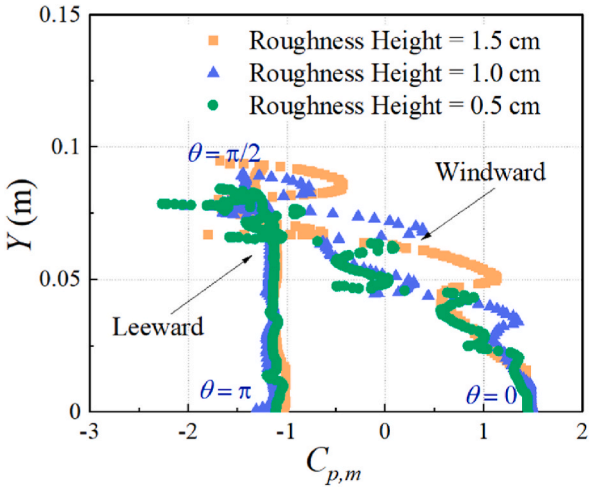

Fig. 13. Time-averaged pressure coefficients for different roughness heights, $U = 0.1$ m/s.

variation of the base pressure coefficient $C_{p,bm}$ is closely related to the flow state. The increased $C_{p,bm}$ in the $k = 0.5$ cm case is a characteristic trait of a critical regime, where $C_{p,bm}$ experiences a sudden jump [6]. However, $C_{p,bm}$ experiences a moderate recovery (larger negative pressure) when the flow enters the supercritical regime. This can be further interpreted by comparing the surface pressure distribution on the SFT at different Reynolds numbers in Fig. 14.

Fig. 14 depicts the $C_{p,m}$ distribution in the Y direction on the SFT upper surface at the slice of the SFT with the largest blockage, for each roughness height at different current speeds (different Re), where some interesting features can be illustrated. Pressures on the windward portion of the SFT at different current speeds are remarkably identical for each roughness height, implying the windward side pressure is independent of Re but determined by the SFT geometry (with roughness elements). Furthermore, the time-averaged base pressure distribution $C_{p,bm}$ is closely linked to the variation of $C_{d,m}$ in Fig. 11 (a). For the $k = 0.5$ cm case, $C_{p,bm}$ increases with increasing current speed in the critical regime, whereas $C_{p,bm}$ experiences a slight increase and a subsequent strong decrease, related to the critical regime and its upper transition for the $k = 1.0$ cm case. However, the dependence of $C_{p,bm}$ on the Re diminishes for the $k = 1.5$ cm case in the completely *trans*-critical regime, inducing a constant $C_{d,m}$ throughout the *trans*-critical regime in Fig. 11 (a).

5.3. *Effect of roughness skewness*

Cases of roughness skewness of -1 and $+1$ for the circular SFT, with equal roughness heights of 1.0 cm, and a staggered arrangement are selected, to investigate the effects of the roughness skewness on the hydrodynamic forces on the SFT. Notice that it is difficult to keep an equal coverage ratio by changing the skewness. In this case, $S_k = -1$ and $+1$ have a coverage ratio of 100% and 50%, respectively (Fig. 4(c)).

Fig. 15 shows $C_{d,m}$ and $C_{l,rms}$ vs. R_e for different roughness skewness. It can be seen that for both cases, $C_{d,m}$ and $C_{l,rms}$ show a steady decrease followed by an increase with increasing Re. However, the minimum value is obtained at a larger Re (around 3.5×10^4) in the $S_k = -1$ case. Due to a larger D_e in the $S_k = -1$ case ($D_{ex} = 0.175$ m), the smaller (smoother) relative roughness parameter makes the drag crisis occur at a higher Re, and the variation of drag is more extensive, compared to the $S_k = +1$ case ($D_{ex} = 0.165$ m). Moreover, it

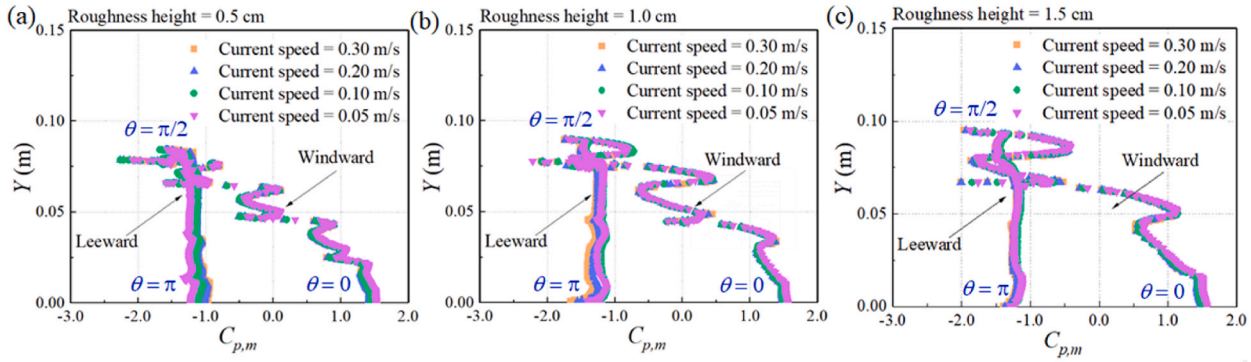

Fig. 14. Time-averaged pressure coefficients for each roughness height with different current speeds. (a) roughness height = 0.5 cm; (b) roughness height = 1.0 cm; (c) roughness height = 1.5 cm.

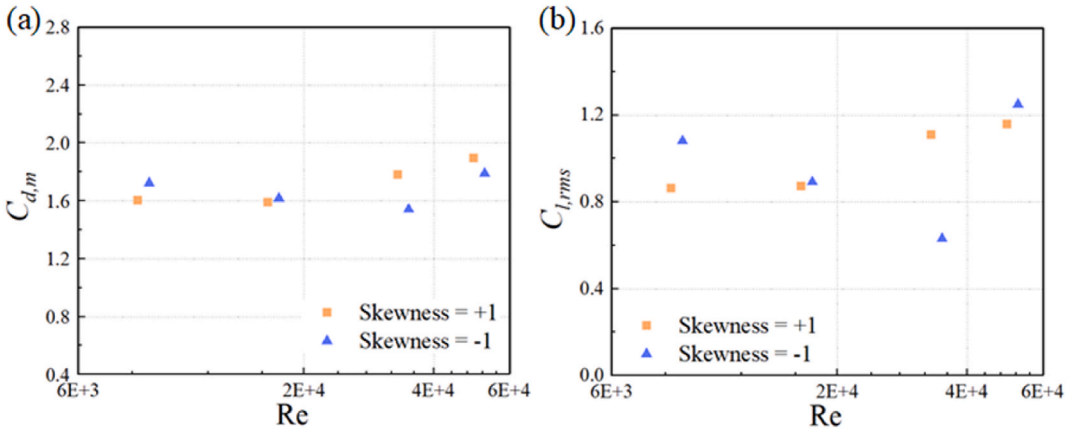

Fig. 15. Simulated hydrodynamic force coefficients for different roughness skewness. (a)$C_{d,m}$ vs R_e; (b)$C_{l,rms}$ vs R_e.

can be observed that $C_{d,m}$ of the $S_k = -1$ case is larger than that of the $S_k = +1$ case in the supercritical regime (Re higher than the drag crisis range).

Fig. 16 shows the mean velocity behind the SFT for different roughness skewness at $U = 0.1$ m/s. The recirculation length in the $S_k = +1$ case is slightly shorter than in the $S_k = -1$ case, and hence, reduces $C_{d,m}$. Notice that the wake width in the $S_k = +1$ case is also narrower, compared to $S_k = -1$ case. This phenomenon can be explained that at the onset of the super-critical regime, due to the pressure gradient increase leeward of the SFT accelerating the flow, the shear layers bend towards the centerline of the wake [45].

Fig. 17 displays the time-averaged pressure coefficient $C_{p,m}$ distribution along the Y direction of the SFT upper surface for a slice of the SFT at the location of the maximum blockage for different roughness skewness with $U = 0.1$ m/s. A significantly larger pressure drop and the subsequent enhancement can be observed in the $S_k = -1$ case on the windward side of the SFT, compared to the $S_k = +1$ case. This is because for an equal blockage area, the reduced roughness height k_s (defined in Eq. (1)) of the $S_k = -1$ case (0.75 cm) is three times larger than of the $S_k = +1$ case (0.25 cm). The mechanism of the pressure change is similar to the roughness height case. The increasing reduced roughness height increases the momentum exchange, causing larger pressure fluctuations. However, at the leeward edge, the $C_{p,m}$ of the $S_k = -1$ case has a lower pressure, which leads to a larger drag.

5.4. *Effect of roughness coverage ratio*

Cases of roughness coverage ratio of 25%, 50%, and 100% for a circular SFT, with equal roughness height of 1.0 cm, staggered arrangement, and roughness skewness of +1 are selected, to investigate the effects of the roughness coverage ratio on the hydrodynamic forces on the SFT (Fig. 4(d)). Fig. 18 shows $C_{d,m}$ and $C_{l,rms}$ vs. Re for different roughness coverage ratios. For coverage ratios of 50% and 100%, both curves show a slight dip at around $Re = 1.65 \times 10^4$, characterized by a transition to a turbulent boundary layer. However, the variation of $C_{d,m}$ and $C_{l,rms}$ in the 50% case is larger than in the 100% case (i.e., increasing rates in the super-critical

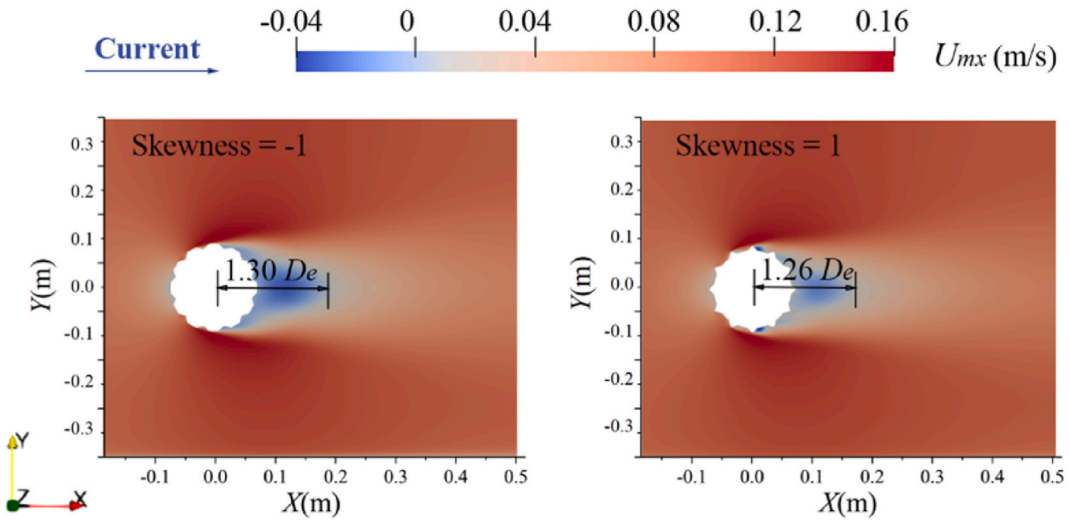

Fig. 16. Mean velocity contours of rough SFTs with different roughness skewness, $U = 0.1$ m/s.

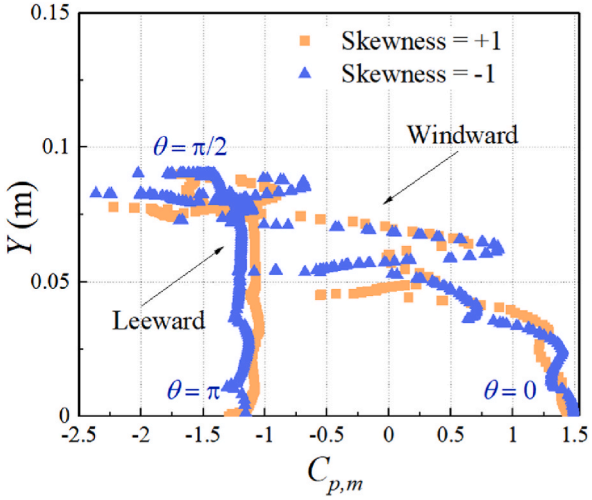

Fig. 17. Time-averaged pressure coefficients for different roughness skewness, $U = 0.1$ m/s.

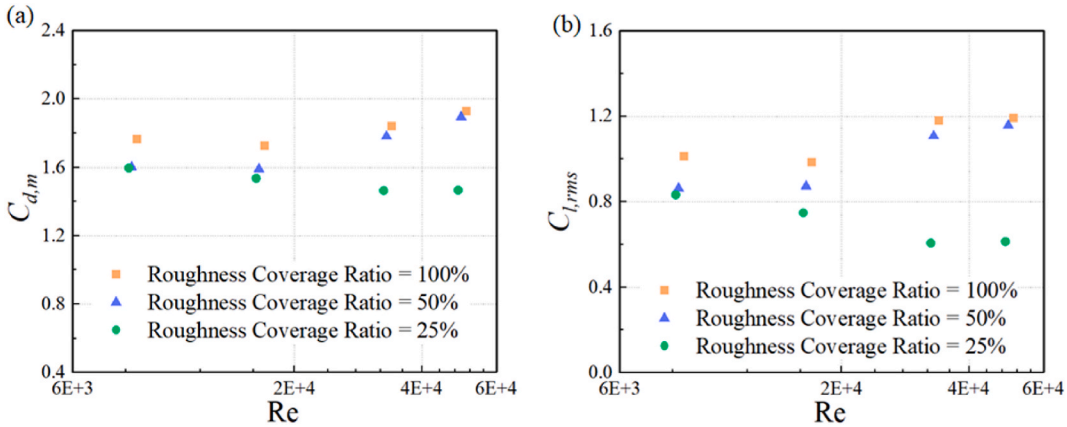

Fig. 18. Simulated hydrodynamic force coefficients for different roughness coverage ratios. (a)$C_{d,m}$ vs R_e; (b)$C_{l,rms}$ vs R_e.

regime are higher). This shows that the drag crisis is less pronounced as the relative roughness parameter increases (i.e., for the 100% coverage case). This is because the flow experiences a relatively weaker momentum exchange near the wall in the large relative roughness case caused by the larger boundary layer thickness, and hence, has a smaller angular location of the separation points than the small relative roughness case (e.g., for the 50% and 25% coverage cases) [43]. For the coverage ratio of 25% however, a continuous decrease and then an almost constant trend are depicted in the $C_{d,m}$ and $C_{l,rms}$ curves, indicating the flow regime might enter from critical to supercritical. It can be seen that $C_{d,m}$ and $C_{l,rms}$ increase with increasing roughness coverage ratio. Similar to the roughness height case, the increase is reduced due to the Reynolds number being on either side of the drag crisis regime.

Fig. 19 shows mean velocity contours behind the SFT for roughness coverage ratios of 25%, 50%, and 100%. Due to the staggered arrangement of roughness elements, the distribution of the roughness elements in the 50% and 100% cases for a slice of the SFT at the location of the maximum blockage has a similar structural pattern. For the sake of clarity, a slice through the center of the roughness element on the apex of the SFT (half of the roughness height) in the X–Y plane is shown. As can be seen, the 25% coverage case has the shortest recirculation length and smallest wake size, which induces the lowest $C_{d,m}$ and $C_{l,rms}$. The 100% coverage case generates the largest wake, and experiences the largest drag and fluctuating lift forces.

Fig. 20 describes the $C_{p,m}$ distribution along the upper surface of the SFT at $U = 0.1$ m/s (at the same slice as in Fig. 19). Due to the presence of more pyramids (roughness elements) in the 100% coverage ratio case, $C_{p,m}$ experiences more jumps; however, in the 25% case, $C_{p,m}$ shows a continuous decline on the windward side of the cross section. For the pressure on the leeward side of the cross section, a larger negative $C_{p,bm}$ is present in the 100% coverage ratio case, due to a larger equivalent diameter and flow separation.

5.5. *Effect of roughness arrangement*

Staggered, horizontal, and vertical roughness layouts for a circular SFT, with equal roughness heights of 1.0 cm, coverage ratio of

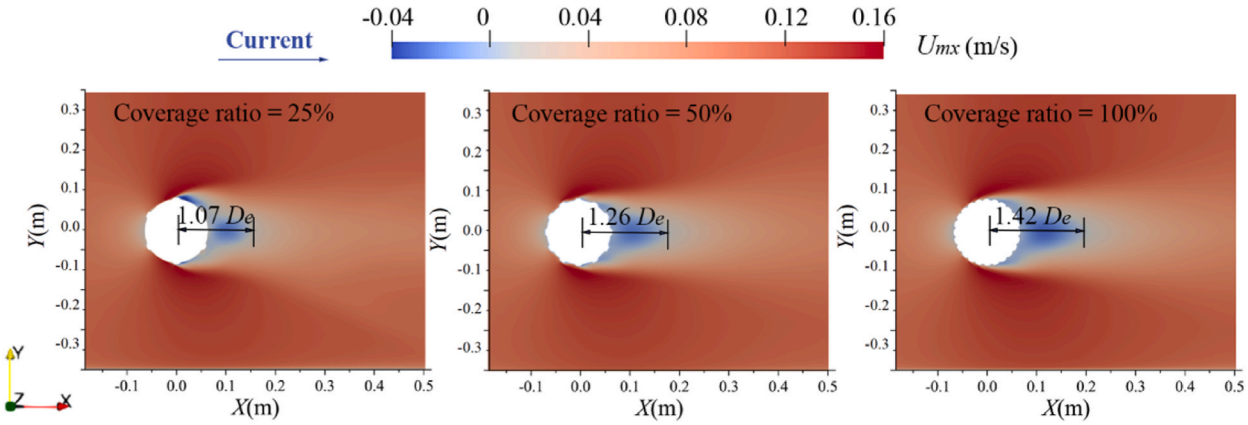

Fig. 19. Mean velocity contours of rough SFTs with different roughness coverage ratios, $U = 0.1$ m/s.

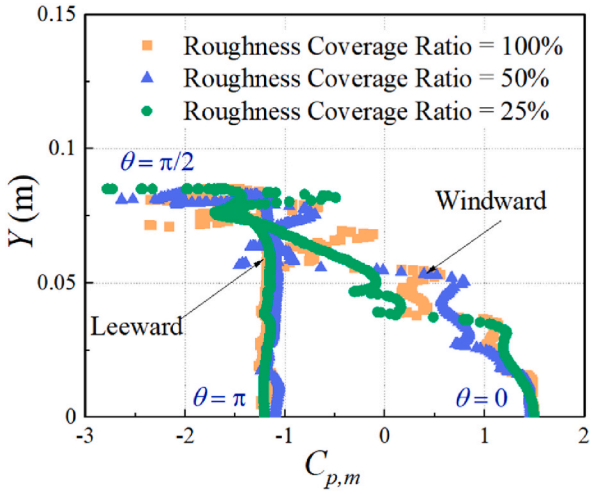

Fig. 20. Time-averaged pressure coefficients for different roughness coverage ratio, $U = 0.1$ m/s.

50%, and roughness skewness of +1 are selected, to investigate the effects of the roughness arrangement on the hydrodynamic forces on the SFT (Fig. 4(e)). Fig. 21 shows $C_{d,m}$ and $C_{l,rms}$ vs. R_e for different roughness arrangements. $C_{d,m}$ and $C_{l,rms}$ show a generally increasing trend with increasing Re for the staggered and horizontal arrangement cases. On the contrary, the vertical arrangement shows a continuous drop with increasing Re, characterized by transition to a turbulent boundary layer. The $C_{d,m}$ and $C_{l,rms}$ in the

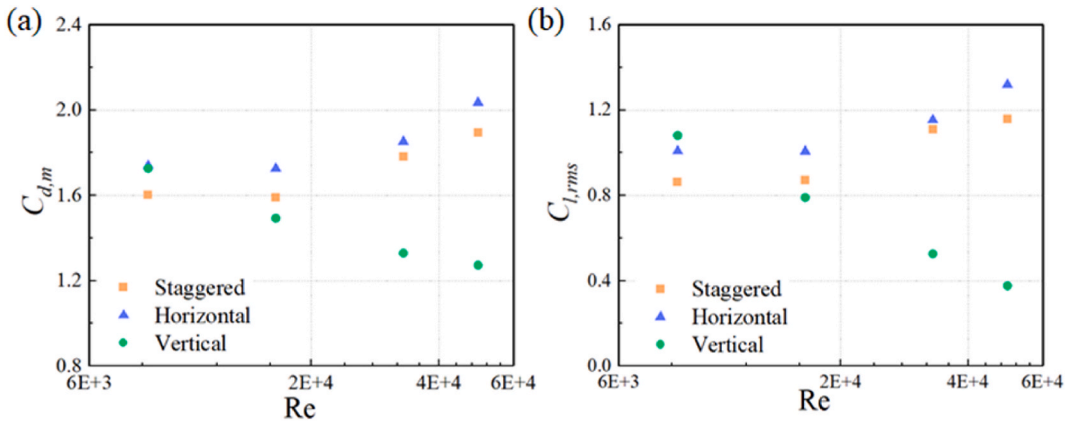

Fig. 21. Simulated hydrodynamic force coefficients for different roughness arrangements. (a)$C_{d,m}$ vs R_e; (b)$C_{l,rms}$ vs R_e.

horizontal arrangement case are amongst the largest at Re $\geq 1.65 \times 10^4$.

Fig. 22 shows mean velocity contours behind SFTs for different roughness arrangements at the transverse slice with largest blockage at $U = 0.1$ m/s. In order to demonstrate the effects of slices with different cut shapes, two slices are shown in the vertical arrangement cases. Interesting to note is that the recirculation length for the staggered and horizontal arrangement cases are similar; while the staggered case presents a narrower wake width, which reduces the drag (i.e., less suction shown in Fig. 23). For the vertical case (Fig. 4(e)), the detached shear layer is found to be farther away from the SFT surface. Furthermore, a wider wake is seen in the Z1 than in the Z2 slice, due to the presence of pyramids. Furthermore, in the Z2 slice, the flow separation point on the smooth cylinder moves further downstream which narrows down the wake width. In addition, the smaller blockage of the smooth cylinder contributes to a further drop in the drag.

Due to the differences in the spatial arrangement of the pyramids, the spatial-temporal averaged (in the Z direction) pressure coefficients $\overline{C_{p,m}}$ at $U = 0.1$ m/s are shown in Fig. 23. On the windward side, the $\overline{C_{p,m}}$ of the horizontal case is seen less smooth, compared to the other two cases. This is because the flow can move between roughness elements in the staggered and vertical cases. However, for the horizontal arrangement, the continuous roughness elements in the Z direction enhance the pressure variation over the SFT surface (e.g., for the position marked in the red block in Fig. 23). Due to the presence of roughness elements, the considerable pressure gradient contributes to an enhancement of the drag. On the leeward side of the SFT, the $\overline{C_{p,m}}$ in the horizontal arrangement case shows the largest suction, while in the vertical and staggered cases $\overline{C_{p,m}}$ does not vary much.

6. Feature importance computation

In the preceding section, we showed that SFT cross-section shape, roughness height, roughness coverage ratio, roughness skewness, and roughness arrangement all affect the hydrodynamic forces on the SFT to different degrees. However, the relationship between the hydrodynamic forces and these influential factors related to roughness is indirect, showing its complexity and nonlinearity in different flow regimes associated with subtle fluid mechanisms such as boundary layer transition and separation, flow reattachment, and wake characteristics. This leads to a need for importance ranking of the roughness parameters, to gain a more direct insight into marine fouling effects on an SFT.

Random forest (RF) is an ensemble technique of machine learning for including a subset of data features at each node to grow a series of decision trees and obtain a final decision by aggregating the results of each decision tree by means of a majority vote [47]. Compared with simple ranking methods such as iterative algorithms [48], RF has demonstrated its capability in dealing with multiple features in computational efficiency, which has been widely adopted in non-linear classification and regression tasks. Furthermore, compared with other machine learning models, RF shows strong advantages in handling imbalanced datasets and being robust against

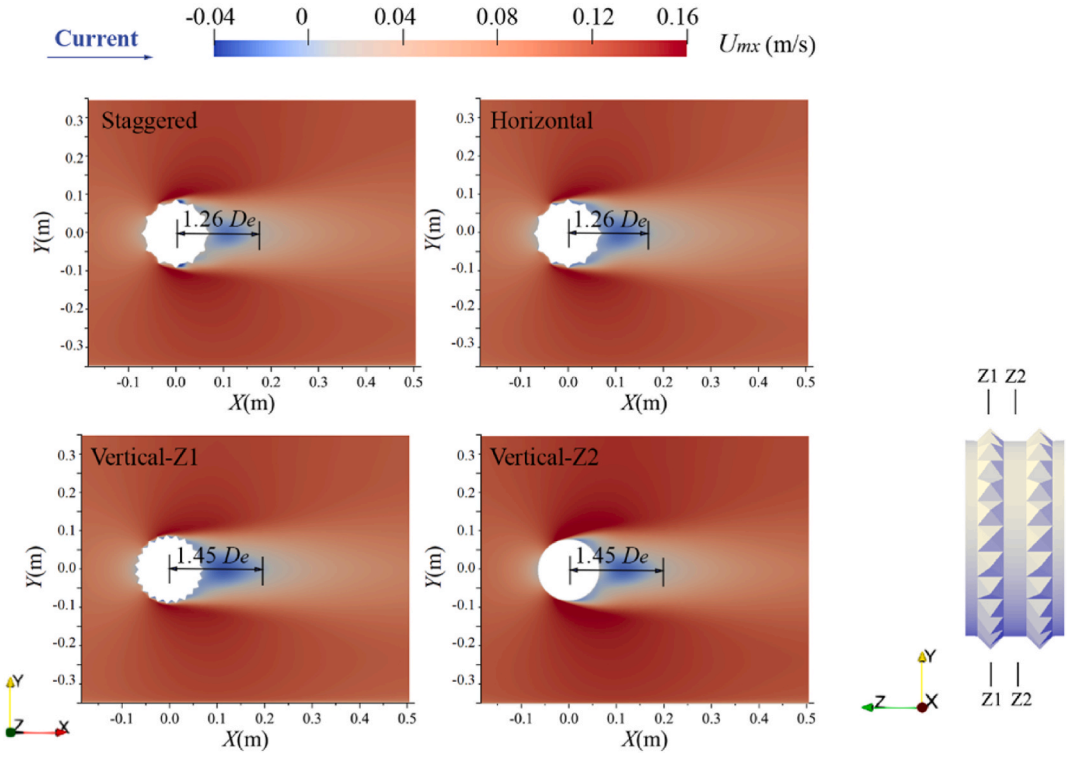

Fig. 22. Mean velocity contours of rough SFTs with different roughness arrangements, $U = 0.1$ m/s.

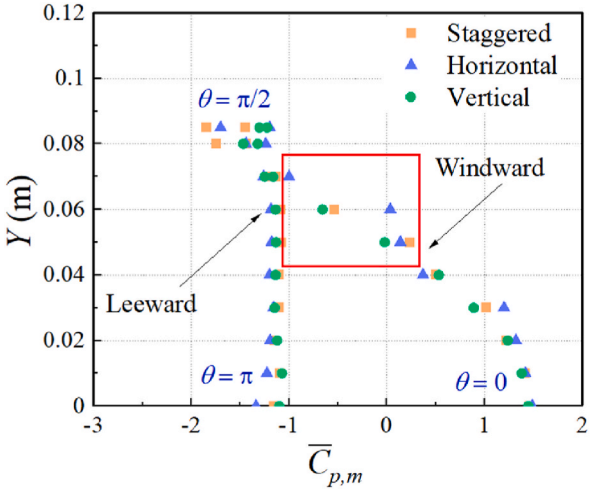

Fig. 23. Spatial-temporal averaged pressure coefficients for different roughness arrangement, $U = 0.1$ m/s.

overfitting [49]. Using an RF, the feature importance can be measured as the mean decrease in impurity (MDI) by computing all the decision trees in the forest. As a computationally efficient classifier for the entropy approximation, the Gini Index or Gini impurity is used to describe the quality of the split of a node on a feature within the decision trees of the RF. The impurity of a node split using Gini impurity is given by

$$\mathrm{Gini}(D) = 1 - \sum_{k=1}^{K} p_k^2 \tag{12}$$

where the collection of data samples is D; p_k is the probability of the kth class ($k = 1, 2, \ldots, K$) in a node.

Followed by weighting each branch based on the baseline probability and summing the weighted Gini index for each split, the Gini index of feature a with the total number of V in a branch can be defined by

$$\mathrm{Gini}(D, a) = \sum_{v=1}^{V} \frac{|D_v|}{|D|} \mathrm{Gini}(D_v) \tag{13}$$

The reduction in impurity is

$$\Delta\mathrm{Gini}(D, a) = \mathrm{Gini}(D) - \mathrm{Gini}(D, a) \tag{14}$$

The feature importance is computed as the mean and standard deviation of accumulation of the impurity decrease within each tree (Gini importance). Consequently, a feature with a higher impurity reduction is deemed to be more important in classification. Conveniently, the RF collecting the feature importance values is implemented in scikit-learn [50], programmed in Python.

Therefore, for the feature importance ranking of roughness parameters for hydrodynamic forces on the SFT, 36 samples with a total of 1000 trees in an RF are trained, and 6 features are ranked by the respective importance measures, including the SFT cross-section shape, roughness height, skewness, coverage ratio, arrangement, and Reynolds number. The target parameters are $C_{d,m}$ and $C_{l,rms}$, respectively. The dataset is split into training and testing subsets. A large number of estimators can reduce the possibility of overfitting

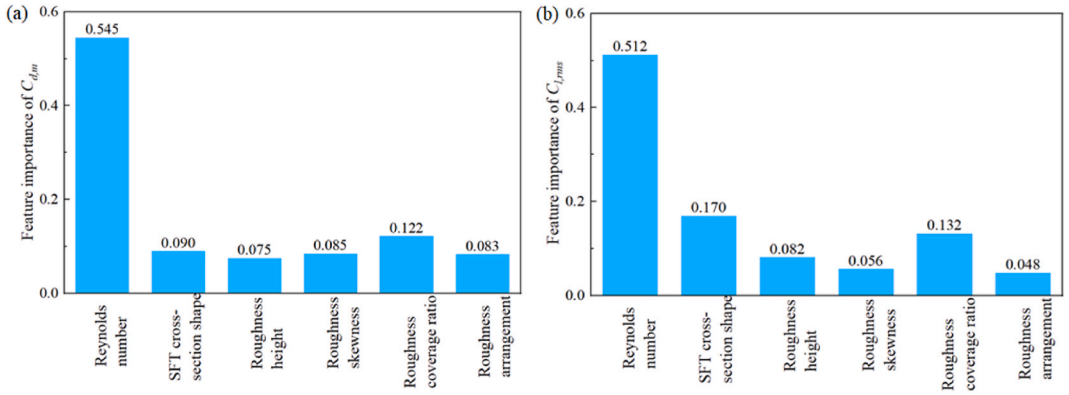

Fig. 24. Results of feature importance for the hydrodynamic forces on the SFT. (a) $C_{d,m}$; (b) $C_{l,rms}$.

and hence increase the prediction accuracy. 70% of the samples are selected as training subsets and the remaining 30% are used as testing subsets. Gini impurity is taken as the function to measure the quality of a split. The nodes are expanded until all leaves contain less than the minimum number of samples required to split an internal node (taken as 2 in this study).

The feature importance for each roughness parameter to the target values of $C_{d,m}$ and $C_{l,rms}$ is shown respectively in Fig. 24. The feature importance values are normalized, and they sum up to 1.0. The results depict that throughout all of the trees considered in the RF, for both $C_{d,m}$ and $C_{l,rms,}$ the Reynolds number is the most important feature, relating to the flow regimes. However, it should be noted that the selected Re range covers the critical to *trans*-critical regimes where the force coefficients on the SFT are highly affected by the involved boundary layer transition and separation, flow reattachment, and wake characteristics. The second important feature for $C_{d,m}$ is the roughness coverage ratio, followed by the SFT cross-sectional shape. The effects of roughness height, roughness arrangement, and roughness skewness on $C_{d,m}$ are similar in the feature importance ranking. For the $C_{l,rms}$, the SFT cross-sectional shape plays an important role, followed by the roughness coverage ratio. The roughness height, roughness skewness, and roughness arrangement are less dominant.

It is interesting to see that for both $C_{d,m}$ and $C_{l,rms}$, roughness coverage ratio and SFT cross-sectional shape rank second and third in importance, respectively. The SFT cross-sectional shape alters the structure geometry and can hence remarkably affects the flow behavior and hydrodynamic forces, while for the lower roughness coverage ratio case, the flow characteristics such as the wake size, recirculation length, and the pressure distribution (in section 5.4) see a significant distinction, compared to the higher roughness coverage ratio case.

7. Conclusions

This paper presents detailed findings of roughness (representing marine fouling) effects on the hydrodynamic forces and flow characteristics of an SFT by means of experimental studies and numerical models with URANS simulations over the range $8.125 \times 10^3 \leq \mathrm{Re} \leq 5.25 \times 10^4$, which encompasses the critical (onset of boundary layer turbulence) and *trans*-critical flow regimes. The numerical results have been validated against experiments by comparing the forces on the SFT and vortex shedding. The effects of roughness parameters including roughness height, skewness, coverage ratio, and spatial arrangement on the hydrodynamic forces under steady currents are investigated. In addition, the force distributions on fouled SFTs with different cross-section shapes (i.e., circular and parametric) are compared. In order to rank the importance of different roughness parameters, a machine learning method (random forest) is applied. The main findings are summarized as follows.

(1) The locations of boundary layer separation on the SFT have been seen in different SFT cross-section shapes, which play a significant role in determining hydrodynamic forces. The SFT cross-section with the parametric shape has a more streamlined shape, thereby inducing later separation and a smaller wake. Therefore, the parametric shape is preferable for its drag force mitigating effects. With an equal blockage height, the parametric shape utilizes space better and has preferable hydrodynamic performance, which is recommended for engineering practice.
(2) The hydrodynamic forces on an SFT increase with increasing roughness height correlating to the blockage area of the SFT and flow state. However, the rate of drag force increase slows down as roughness height increases. The presence of pyramids with increasing roughness height generates larger pressure gradients and transfers more momentum, leading to larger fluctuations of surface pressure at the windward edge. In addition, the energy dissipation also increases with increasing roughness height.
(3) The relative roughness parameter is a crucial factor in the roughness skewness cases, which leads to a shift in the critical Reynolds number for boundary layer turbulence. As skewness decreases, the SFT becomes smoother, accompanied by a drag crisis occurring at a higher Re and a more extensive force coefficient variation. Furthermore, in the supercritical regime, the drag coefficient of the SFT decreases with decreasing roughness skewness.
(4) The hydrodynamic forces increase with increasing roughness coverage ratio, while the trend flattens as roughness coverage ratio increases. An SFT with a lower coverage ratio (such as 25%) can effectively shorten the flow recirculation length and wake width, and hence, dramatically reduce hydrodynamic forces.
(5) In the case of the presence of different roughness arrangements, the roughness patterns interact and cause different behaviors in the nearfield wake. The horizontal roughness distribution generally induces the largest hydrodynamic forces throughout the selected Re range, followed by a staggered arrangement. The flow around the SFT with vertically distributed pyramids remains at the critical regime, generating the minimum hydrodynamic forces.
(6) Random forest is an effective method in dealing with non-linear relationships for feature importance ranking. The flow regime affects the hydrodynamic forces more than the roughness parameters do. In addition, the SFT cross-section shape and roughness coverage ratio are crucial factors affecting hydrodynamic forces.

The current study presents marine fouling effects on SFTs subject to steady currents in detail for the first time. These findings indicate the roughness effects can propagate far into the wake area and affect the hydrodynamic forces and further dynamic response of the SFT. The evaluated findings of hydrodynamic force in relation to roughness parameters can provide references for dynamic response, reliability analysis, and the design optimization of SFTs.

It should be noted that the regular pyramidal roughness only very roughly represents actual marine fouling organisms. Roughness elements due to real marine deposition are highly related to fouling morphology, texture, density, and growth type (i.e., hard, soft, kelp). A more realistic roughness pattern with random distribution should be included in further hydrodynamic investigation for an SFT.

Declaration of competing interest

The authors declare that they have no known competing financial interests or personal relationships that could have appeared to influence the work reported in this paper.

Data availability

The data that has been used is confidential.

Acknowledgement

The study presented in this paper was conducted in the submerged floating tunnel research project funded by China Communications Construction Company Ltd. (CCCC). Partial funding for reporting comes from a Cooperative Institute for Great Lakes Research (CIGLR) postdoctoral fellowship.

References

[1] P. X. Zou, J. D. Bricker, and W. S. J. Uijttewaal, "Impacts of extreme events on hydrodynamic characteristics of a submerged floating tunnel," Ocean Eng., vol. 218, 2020, doi: 10.1016/j.oceaneng.2020.108221.
[2] Zou PX, Bricker JD, Uijttewaal WSJ. The impacts of internal solitary waves on a submerged floating tunnel. Ocean Eng 2021;238:109762.
[3] P. X. Zou, J. D. Bricker, L. Z. Chen, W. S. J. Uijttewaal, and C. Simao Ferreira, "Response of a submerged floating tunnel subject to flow-induced vibration," Eng Struct, vol. 253, 2022, doi: 10.1016/j.engstruct.2021.113809.
[4] Zeinoddini M, Bakhtiari A, Ehteshami M, Seif MS. Towards an understanding of the marine fouling effects on VIV of circular cylinders: response of cylinders with regular pyramidal roughness. Appl Ocean Res 2016;59. https://doi.org/10.1016/j.apor.2016.05.013.
[5] Schoefs F, et al. Fractal dimension as an effective feature for characterizing hard marine growth roughness from underwater image processing in controlled and uncontrolled image environments. J Mar Sci Eng 2021;9(12). https://doi.org/10.3390/jmse9121344.
[6] N. Paul van Hinsberg, "Mean and unsteady loading on square prisms with rounded edges: hard marine growth, incidence, and Reynolds number effects," Mar Struct, vol. 75, 2021, doi: 10.1016/j.marstruc.2020.102886.
[7] F. Nobakht-Kolur, M. Zeinoddini, M. M. A. Harandi, F. A. Abi, and P. Jadidi, "Effects of soft marine fouling on wave-induced forces in floating aquaculture cages: physical model testing under regular waves," Ocean Eng., vol. 238, 2021, doi: 10.1016/j.oceaneng.2021.109759.
[8] Wright C, Murphy J, Pakrashi V. The dynamic effects of marine growth on a tension moored floating wind turbine. In: Progress in renewable energies offshore - proceedings of 2nd international conference on renewable energies offshore. RENEW; 2016. https://doi.org/10.1201/9781315229256-85. 2016.
[9] Shi W, Park HC, Baek JH, Kim CW, Kim YC, Shin HK. Study on the marine growth effect on the dynamic response of offshore wind turbines. Int J Precis Eng Manuf 2012;13(7). https://doi.org/10.1007/s12541-012-0155-7.
[10] Ameryoun H, Schoefs F, Barillé L, Thomas Y. Stochastic modeling of forces on jacket-type offshore structures colonized by marine growth. J Mar Sci Eng 2019;7 (5). https://doi.org/10.3390/jmse7050158.
[11] Bearman PW, Harvey JK. Control of circular cylinder flow by the use of dimples. AIAA J 1993;31(10). https://doi.org/10.2514/3.11844.
[12] Zhou B, Wang X, Gho WM, Tan SK. Force and flow characteristics of a circular cylinder with uniform surface roughness at subcritical Reynolds numbers. Appl Ocean Res 2015;49. https://doi.org/10.1016/j.apor.2014.06.002.
[13] Duarte Ribeiro J. Effects of surface roughness on the two-dimensional flow past circular cylinders I: mean forces and pressures. J Wind Eng Ind Aerod 1991;37 (3). https://doi.org/10.1016/0167-6105(91)90014-N.
[14] A. Marty et al., "Experimental study of hard marine growth effect on the hydrodynamical behaviour of a submarine cable," Appl Ocean Res, vol. 114, 2021, doi: 10.1016/j.apor.2021.102810.
[15] Theophanatos A, Wolfram J. Hydradynamic loading on macro-roughened cylinders of warious aspect ratios. J Offshore Mech Arctic Eng 1989;111(3). https://doi.org/10.1115/1.3257150.
[16] West GS, Apelt CJ. The effects of tunnel blockage and aspect ratio on the mean flow past a circular cylinder with Reynolds numbers between 104 and 105. J Fluid Mech 1982;114. https://doi.org/10.1017/S0022112082000202.
[17] Roshko A. Experiments on the flow past a circular cylinder at very high Reynolds number. J Fluid Mech 1961;10(3). https://doi.org/10.1017/S0022112061000950.
[18] Blackburn HM, Melbourne WH. The effect of free-stream turbulence on sectional lift forces on a circular cylinder. J Fluid Mech 1996;306. https://doi.org/10.1017/S0022112096001309.
[19] Jusoh I, Wolfram J. Effects of marine growth and hydrodynamic loading on offshore structures. J. Mek. 1996;1.
[20] Achenbach E, Heinecke E. On vortex shedding from smooth and rough cylinders in the range of Reynolds numbers 6×103 to 5×106. J Fluid Mech 1981;109 (12). https://doi.org/10.1017/S002211208100102X.
[21] Abdelaziz M, Djenidi L, Ghayesh MH, Chin R. A new equivalent sand grain roughness relation for two-dimensional rough wall turbulent boundary layers. J Fluid Mech 2022;940:A25. https://doi.org/10.1017/jfm.2022.242.
[22] Achenbach E. Influence of surface roughness on the cross-flow around a circular cylinder. J Fluid Mech 1971;46(2). https://doi.org/10.1017/s0022112071000569.
[23] Demirel YK, Uzun D, Zhang Y, Fang HC, Day AH, Turan O. Effect of barnacle fouling on ship resistance and powering. Biofouling 2017;33(10). https://doi.org/10.1080/08927014.2017.1373279.
[24] Schultz MP. Effects of coating roughness and biofouling on ship resistance and powering. Biofouling 2007;23(5). https://doi.org/10.1080/08927010701461974.
[25] Fuss FK. The effect of surface skewness on the super/postcritical coefficient of drag of roughened cylinders. Procedia Eng 2011;13. https://doi.org/10.1016/j.proeng.2011.05.086.
[26] P. Zou, J. Bricker, and W. Uijttewaal, "Optimization of submerged floating tunnel cross section based on parametric Bézier curves and hybrid backpropagation - genetic algorithm," Mar Struct, vol. 74, 2020, doi: 10.1016/j.marstruc.2020.102807.
[27] Zou PX, Bricker JD, Uijttewaal W. A parametric method for submerged floating tunnel cross-section design. In: Proceedings of the international offshore and polar engineering conference; 2020.
[28] P.X. Zou, N. Ruiter, W. S. J. Uijttewaal, X. X. Chen, D. J. Peters, and J. D. Bricker, "Experimental study of surface roughness effects on hydrodynamic characteristics of a submerged floating tunnel," Appl Ocean Res, [under review].
[29] Watson KP, Granger RA. Hydrodynamic effect of a satellite transmitter on a juvenile green turtle (Chelonia mydas). J Exp Biol 1998;201(17). https://doi.org/10.1242/jeb.201.17.2497.
[30] Greenshields C. OpenFOAM User Guide Version v2112. 2021. 35.
[31] D. H. P. C. C. (DHPC. DelftBlue Supercomputer (Phase 1)." 2022. [Online]. Available: https://www.tudelft.nl/dhpc/ark:/44463/DelftBluePhase1.

[32] Zou P, Bricker JD, Uijttewaal W. Submerged floating tunnel cross-section analysis using a transition turbulence model. J Hydraul Res 2021. https://doi.org/10.1080/00221686.2021.1944921.
[33] Fluent A. Ansys fluent theory guide. USA: ANSYS Inc.; 2013.
[34] Langtry RB, Menter FR. Correlation-based transition modeling for unstructured parallelized computational fluid dynamics codes. AIAA J 2009. https://doi.org/10.2514/1.42362.
[35] Ansys F. ANSYS fluent theory guide 19.1. Canonsburg, PA: ANSYS; 2019.
[36] il Seo S, suk Mun H, ho Lee J, ha Kim J. Simplified analysis for estimation of the behavior of a submerged floating tunnel in waves and experimental verification. Mar Struct 2015. https://doi.org/10.1016/j.marstruc.2015.09.002.
[37] Z. Wu, D. Wang, W. Ke, Y. Qin, F. Lu, and M. Jiang, "Experimental investigation for the dynamic behavior of submerged floating tunnel subjected to the combined action of earthquake, wave and current," Ocean Eng., vol. 239, 2021, doi: 10.1016/j.oceaneng.2021.109911.
[38] Deng S, Ren H, Xu Y, Fu S, Moan T, Gao Z. Experimental study of vortex-induced vibration of a twin-tube submerged floating tunnel segment model. J Fluid Struct 2020. https://doi.org/10.1016/j.jfluidstructs.2020.102908.
[39] Reichl P, Hourigan K, Thompson MC. Flow past a cylinder close to a free surface. J Fluid Mech 2005;533. https://doi.org/10.1017/S0022112005004209.
[40] Wilcox DC. Turbulence modeling for CFD. 1993.
[41] Allen HJ, Vincenti WG. Wall interference in a two-dimensional-flow wind tunnel, with consideration of the effect of compressibility. NACA Rep. 1944;30(782).
[42] Maskell EC. A theory of blockage effects on bulff bodies and stalled wings in a closed wind tunnel. Her Majesty's Station. Off.; 1965.
[43] Sumer BM, Fredsøe J. Hydrodynamics around cylindrical structures. revised edition 2006. https://doi.org/10.1142/6248.
[44] Schewe G. On the force fluctuations acting on a circular cylinder in crossflow from subcritical up to transcritical Reynolds numbers. J Fluid Mech 1983;133. https://doi.org/10.1017/S0022112083001913.
[45] Rodríguez I, Lehmkuhl O, Chiva J, Borrell R, Oliva A. On the flow past a circular cylinder from critical to super-critical Reynolds numbers: wake topology and vortex shedding. Int J Heat Fluid Flow 2015;55. https://doi.org/10.1016/j.ijheatfluidflow.2015.05.009.
[46] Sallet DW. Lift force due to von karman's vortex wake. J Hydronautics 1973. https://doi.org/10.2514/3.62951.
[47] Breiman L. 2001 4_Method_Random_Forest. Mach Learn 2001;45(1).
[48] Bromaghin JF. Bels: backward elimination locus selection for studies of mixture composition or individual assignment. Mol. Ecol. Resour. 2008;8(3). https://doi.org/10.1111/j.1471-8286.2007.02010.x.
[49] Jalal N, Mehmood A, Choi GS, Ashraf I. A novel improved random forest for text classification using feature ranking and optimal number of trees. J. King Saud Univ. Inf. Sci.; 2022.
[50] Pedregosa F, et al. Scikit-learn: machine learning in Python. J Mach Learn Res 2011;12:2825–30.